Heliyon 9 (2023) e21124

Contents lists available at ScienceDirect

Heliyon

journal homepage: www.cell.com/heliyon

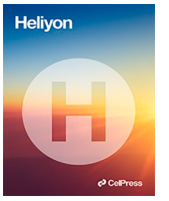

Tailored synthesis of iron oxide nanoparticles for specific applications using a statistical experimental design

María José Inestrosa-Izurieta *, Diego Vilches, Julio I. Urzúa

Centro de Materiales para la Transición y Sostenibilidad Energética, Comisión Chilena de Energía Nuclear, 7600713, Santiago, Chile

ARTICLE INFO

Keywords:
Nanoparticles
Superparamagnetic: magnetite
Co-precipitation method
Experimental design

ABSTRACT

For this work, iron oxide nanoparticles are synthesized by the co-precipitation method with stoichiometric amounts of Fe^{2+} and Fe^{3+} salts in a 1:2 ratio in distilled water and the pH is raised by adding an aqueous ammonia solution by controlled dripping. Nanoparticles precipitating after the reaction time are magnetically filtered and stored in ethanol for further analysis. Superparamagnetic Fe_3O_4 nanoparticles with a slight deviation from the stoichiometry are obtained, with sizes between 7.4 and 12.8 nm and saturation magnetization between 40 and 78 emu/gr. At pH 6, rod-shaped nanoparticles are obtained in addition to spherical ones. With a statistical design, it is shown how the morphological, structural and magnetic properties of the resulting nanoparticles can be manipulated by the synthesis parameters, offering many possibilities to tailor the materials to a wide range of applications.

1. Introduction

Magnetic nanoparticles (MNP) are versatile materials that have practical uses in fields like magnetic recording, drug delivery, bioimaging, hyperthermia, photothermal therapy, sensors, water purification, and magnetic separation [1–11]. Different kinds of iron oxide nanoparticles are promising, with Fe_3O_4 and γ-Fe_2O_3 being the most extensively explored [12]. In particular, magnetite (Fe_3O_4) displays the highest level of magnetism and saturation magnetization (Ms) at room temperature, measuring 84 emu/g.

One important aspect of nanoscale materials is their significantly larger surface area relative to bulk matter, which leads to distinct physicochemical properties. Specifically, magnetite nanoparticles with diameters less than 30 nm demonstrate superparamagnetic behavior, exhibiting a strong response to external magnetic fields with no residual magnetization and reduced agglomeration tendencies [4].

For most applications, nanoparticles need to have uniform size and shape while being well dispersed in a solvent. The synthesis method typically controls the size and shape of the nanoparticles. Various techniques are available to synthesize magnetite nanoparticles, including co-precipitation, thermal decomposition, hydrothermal and solvothermal, sol-gel and polyol, microemulsion, electrospray, sonochemical and microwave-assisted, and biosynthesis methods [2,8–14]. Due to its rapid processing, efficient reaction conditions, simplicity and high yield, wet chemical synthesis by co-precipitation is widely used [13]. In general, novel phenomena can be achieved by careful control of particle size and dispersion in composites. Accordingly, synthesis represents the critical parameter in developing crystalline iron-oxide polymorphs that have desirable and distinctive properties well-suited for various technological applications [15].

* Corresponding author.
E-mail address: mariajose.inestrosa@cchen.cl (M.J. Inestrosa-Izurieta).

https://doi.org/10.1016/j.heliyon.2023.e21124
Received 18 August 2023; Received in revised form 2 October 2023; Accepted 16 October 2023
Available online 18 October 2023

While numerous articles discuss the co-precipitation synthesis of magnetite, there is no consensus regarding the regulation of properties through synthesis parameters. Instead, there is a preference for the conventional use of the Massart procedure [16], accompanied by slight modifications that do not account for parameter interrelationships. Additionally, a particular case study with a statistical approach that covers only some of these parameters has been considered [13].

The aim of this study is to synthesize iron oxide nanoparticles while varying conditions, such as the drip rate of the alkaline solution. These modifications may affect the properties of the nanoparticles, leading to differences in the resulting product. It is, therefore, crucial to analyze the impact of such changes on the properties of the nanoparticles.

We used a statistical approach to describe and forecast the influence of certain vital synthesis parameters, which is crucial in producing tailored MNPs for numerous applications. We examined the morphological, structural, and magnetic characteristics of the synthesized magnetite nanoparticles. A model was generated to predict particle properties accurately within the studied range of synthesis parameters, offering numerous possibilities for material customization across a wide range of applications.

2. Materials and methods

2.1. General information

This study optimized nanoparticle synthesis variables via iron co-precipitation using the Box-Behnken design (BBD) and response surface methodology (RSM). Magnetic properties of MNP were characterized with a vibrating sample magnetometer (VSM), whereas morphological, chemical, and structural properties were analyzed by transmission electron microscopy (TEM) and powder X-ray diffraction (XRD). All experiments were conducted using STATGRAPHICS Centurion XVI software, based on the "design of experiments" (DoE) methodology. The resulting models were further validated through additional experiments.

2.2. Experimental design and statistical analysis

To identify the optimal combination of co-precipitation variables for synthesizing MNP, we utilized a three-level, four-factor Box-Behnken design (BBD) based on the preliminary range of co-precipitation variables established through single-factor experiments. The BBD constitutes a rotating spherical response surface that features a center point, as well as midpoints between the corners, all of which are circumscribed on a sphere. This design, determined by the process requirements, can optimize multiple chemical and physical processes with a suitable number of experiments [17–20].

We selected the alkalization drip rate (V_{NH4}), reaction time (T_{res}), temperature (Temp), and stirring rate (Stirr) as the parameters of interest. All syntheses were executed in a precisely controlled reaction setup.

The Box-Behnken design was then applied to an expanded study range that covered the preliminary parameters. Thus, the V_{NH4} factor was evaluated between 10 and 90 ml/h, T_{res} between 10 and 50 min, Temp between 30 and 90 °C, and Stirr between 300 and

Table 1
BBD experiments parameters.

	PH	V_NH4	T_reac	Temp	Stirr
BBD01	9	50	30	30	300
BBD02	9	50	30	60	600
BBD03	9	10	30	30	600
BBD04	9	10	30	60	900
BBD05	9	10	30	90	600
BBD06	9	90	10	60	600
BBD07	9	10	30	60	300
BBD08	9	50	30	90	300
BBD09	9	50	30	60	600
BBD10	9	90	30	60	300
BBD11	9	50	50	30	600
BBD12	9	10	10	60	600
BBD13	9	90	30	90	600
BBD14	9	90	50	60	600
BBD15	9	50	30	90	900
BBD16	9	50	50	90	600
BBD17	9	50	50	60	900
BBD18	9	50	30	30	900
BBD19	9	50	50	60	300
BBD20	9	50	30	60	600
BBD21	9	90	30	60	900
BBD22	9	50	10	30	600
BBD23	9	50	10	90	600
BBD24	9	90	30	30	600
BBD25	9	50	10	60	300
BBD26	9	10	50	60	600
BBD27	9	50	10	60	900

900 rpm (Table 1).

The chosen variables for synthesizing the nanoparticles were: mean diameter of the resulting nanoparticles (NP_{size} and NP_{xrd}), expressed in nm; the distribution of the nanoparticle sizes (Disp), expressed as a percentage of NP_{size}; the agglomeration of the nanoparticles (Aglo), expressed in arbitrary units.; the saturation magnetization (M_s), expressed in emu/gr; the coercive field (H_c), expressed in Oerted; the remnant magnetization (M_r), expressed in emu/gr; and the oxidation state of magnetite (3-x of $F_{3-x}O_4$). To minimize the effects of unanticipated variables, all experiments were conducted in random order.

The generalized polynomial model of the second order that is used in response surface analysis is described in Eq. (1).

$$Y = A_0 + \sum_{i=1}^{n} A_i X_i + \sum_{i=1}^{n} A_{ii} X_i^2 + \sum_{i=1}^{n-1} \sum_{j=2}^{n} A_{ij} X_i X_j \quad (1)$$

where Y represents the response variable; A_o, A_i, A_{ii}, and A_{ij} are the regression coefficients for the intercept, linear, quadratic, and interaction terms, respectively; and X_i and X_j are the independent variables where i is not equal to j. A positive or negative sign indicates a direct or inverse effect of the variable on the target, respectively. The models were used to assess the impact of each independent variable on the responses.

STATGRAPHICS Centurion XVI (version 16.1.03) was used for the analysis of the experimental design and the calculation of the predicted data. The effectiveness of the polynomial model equations was measured via the coefficient of determination R2 using analysis of variance (ANOVA). This method was utilized to assess variable impacts, interactions, and the statistical significance of the models. The optimal synthesis conditions were estimated through regression analysis and 3D response surface plots. To confirm the experimental statistical strategies' validity, we conducted three additional experiments. (See Ref. [21] for more information on experimental design and statistical analysis.).

In general, our results are statistically significant for the resulting effects, which indicates that the fitted models explain approximately 70 % or more of the variability in all the cases.This implies that the data have high variability, but still show a significant trend. This trend indicates that even though the data points are far from the regression line, the predictor variable is still providing information about the response.

2.3. Syntesis of iron oxide nanoparticles

In theory, the co-precipitation synthesis method entails the addition of a base, typically NaOH or NH_3 (aq), to a distilled water solution containing Fe^{+2} and Fe^{+3} salts in a 1:2 stoichiometric ratio, which matches the stoichiometry for magnetite precisely. This process aims to produce magnetite nanoparticles with high purity. Eq. (2) shows the resulting reaction.

$$Fe^{+2} + 2Fe^{+3} + 8OH^- \rightarrow Fe_3O_4 + 4H_2O \quad (2)$$

In this work, a specific set of 27 magnetite NPs samples were synthesized by co-precipitation according to a Box-Behnken experimental design.

For each synthesis, 486 mg of $FeCl_3.6.H_2O$ and 250 mg of $FeSO_4.7.H_2O$ were specifically diluted in a total of 60 mL of distilled water. The resulting mixture was added to a three-necked glass flask with an additional 60 ml of heated distilled water, reaching the specified temperature on a hotplate in a silicone bath. The final volume of the solution was 120 ml. The system is used sealed with septum plugs through which a constant flow of N_2 is injected to prevent oxidation during the synthesis. At the same time, the mixture is stirred at Stirr speed with a mechanical PTFE stirrer with four 45° angled blades. Once the desired temperature has been reached, a 28 % ammonia solution is injected with a programmable syringe pump at V_{NH4} until a pH of 9 is achieved. The system maintains these conditions until the indicated T_{res} time has elapsed. The resulting solution is magnetically filtered using a neodymium permanent magnet. Then, 100 ml of deionized water is added again to wash the nanoparticles, followed by sonication for 1 min. This process is repeated thrice, and in the final step, the water is replaced by 40 ml of ethanol. Finally, each sample is labeled and stored in two clear glass vials with a capacity of 20 mL. One of the vials is then oven-dried at 30 °C.

It is important to note that all samples were replicated consistently to achieve accurate results for proper analysis.

2.4. Characterization of nanoparticles

2.4.1. TEM

Transmission electron microscopy was utilized to assess the morphology of the nanoparticles. Since the nanoparticles are agglomerated, the measure of the average size of each sample were made measuring hundreds of nanoparticle diameters individually in multiple TEM images. These data are used to create a histogram, which is finally satisfactorily distributed according to a function *f* (D) described by a log-linear distribution (Eq. (3)).

$$f(D) = \frac{1}{\sqrt{2\pi}\sigma D} \exp\left\{ -\frac{\ln^2(D/D_0)}{2\sigma^2} \right\} \quad (3)$$

where D_0 is the mean value of particle diameter and σ^2 is the variance.

2.4.2. XRD

Powder XRD patterns were obtained with PAN analytical, X'pert PRO using 40 kV, 30 mA, Cu Kα radiation (λ = 1.5405 Å) in the scanning range of 10°–65° (2θ).

X-ray diffraction was used for structural characterization, considering that the patterns provide information on particle size while the relative intensities of the peaks provide the information to identify the crystalline phase.

The Debye-Scherrer equation (Eq. 4) is a widely used tool to calculating the mean crystallite size, considering the broadening of a peak in the spectrum at half height.

$$D = \frac{k\lambda}{B\cos\Theta} \tag{4}$$

where D is the average diameter of the nanoparticles, k is Sherrer's constant which can be assumed to be 0.89 for magnetite, B is the full width at half maximum or the broadening of the diffraction line in radians, λ is the wavelength of the X-ray used, and 2Θ is the diffraction angle.

2.4.3. VSM

The magnetic properties of MNP were characterized using a vibrating sample magnetometer, wich provides information on the magnetic moment as a function of the applied magnetic field. This information represents the corresponding magnetization curve, wich was used to obtain the saturation magnetization (M_s), remnant magnetization (M_r) and coercivity (H_c).

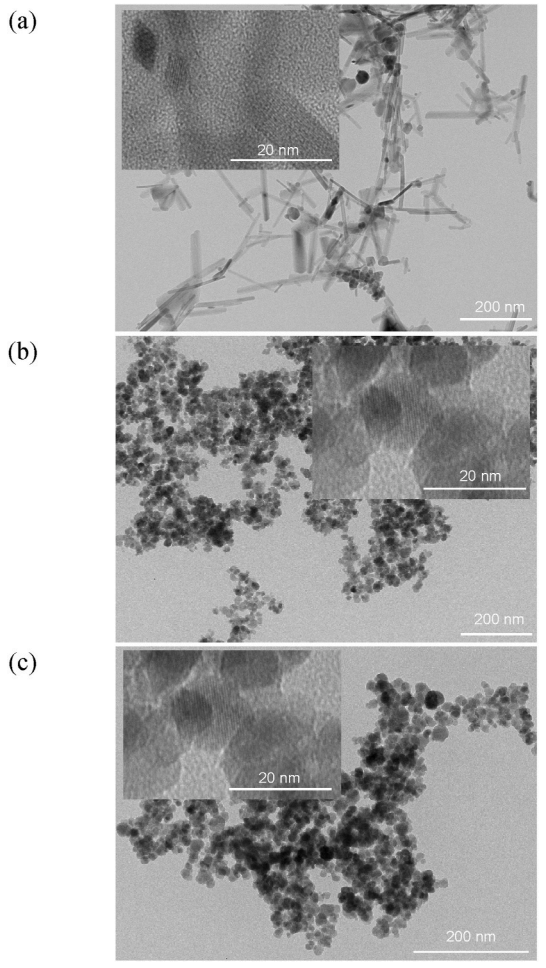

Fig. 1. TEM images of the nanoparticles for (a) pH 6, (b) pH 9, (c) pH 11.

3. Results and discussion

3.1. Effect of the pH on iron oxide

In a preliminary analysis, varying the pH, we obtained specific results for pH 6, 9, and 11. In the TEM images, Fig. 1 (a, b, c), it can be seen that in all three cases spherical nanoparticles were synthesized, except that in the case of pH 6, that were observed mixed with nanorods. In the TEM images it is also possible to visualize the lattice spacing of individual nanoparticles for each case. In Fig. 1, part (a) displays a nanorod having a lattice spacing of 0.46 and 0.18 nm that corresponds to twice the (200) and (211) goethite planes, respectively. Moreover, there is a rhombohedron that can be visualized with a lattice spacing of 0.44 and 0. Three types of nanoparticles were identified through XRD diffractogram analysis of the samples, as shown in Fig. 2 (a, b): (a) Rods measuring 15 nm corresponded to the (210) and (310) planes of goethite, each occurring twice; (b) A nanoparticle with a lattice spacing of 0.58 nm corresponds to two (200) magnetite planes; and (c) Another nanoparticle with a lattice spacing of 0.52 nm corresponds to 2 times (311) magnetite plane. Therefore, it is possible to determine that the identified rods are made of goethite.

This study presents a clear demonstration of the reaction and formation pathways in the co-precipitation of magnetite nanoparticles. The addition of base to the iron solution resulted in the nuclei and growth of nanoparticles passing through the goethite phase before reaching the magnetite phase, corroborating previous findings [13,22–25]. In the diffractograms obtained for pH9 and pH11 it is possible to observe that the peak positions are slightly shifted towards higher 2θ values, indicating that the lattice parameter is contracted potentially due to the eventual oxidation of magnetite (This will be discussed later in this article.). On the other hand, the Ms measurements obtained for the samples (Fig. 3), with values corresponding to 41.5, 77.8 and 68.2 emu/g, for the samples at pH 6, 9 and 11, respectively. The magnetic properties of the nanoparticles decrease as pH increases above 9. Thus, it is evident that pH plays a critical role in the formation pathway, rather than a specific ammonia dilution (molar ratio between ammonia and iron ions) as stated in a recent paper [3].

Based on the data, pH 9 was chosen as it guarantees the creation of a nanoparticulate material with exceptional magnetic properties [26]. Likewise, after some tests prior to those presented in this work, in which an ambient environment was used, with the presence of oxygen, vs. a controlled environment, with nitrogen injection, it was decided to work in a controlled environment in order to generate an oxygen-free environment to avoid uncontrolled oxidation of the material.

It should be noted that even the manipulation of the synthesis parameters for the specific obtention of goethite could be particularly useful in some applications taking advantage of its shape [3].

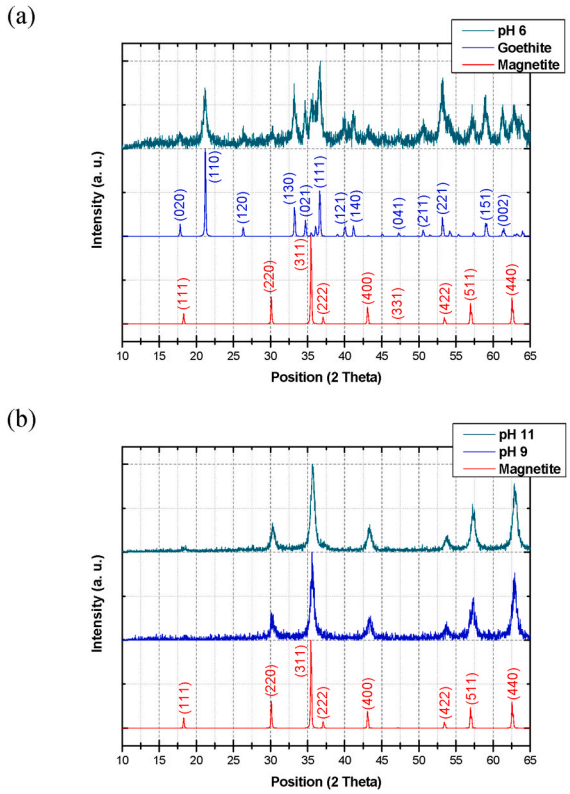

Fig. 2. XRD diffractograms of the resulting nanoparticles for (a) pH 6, (b) pH 9 and pH 11, with their structural pattern identification.

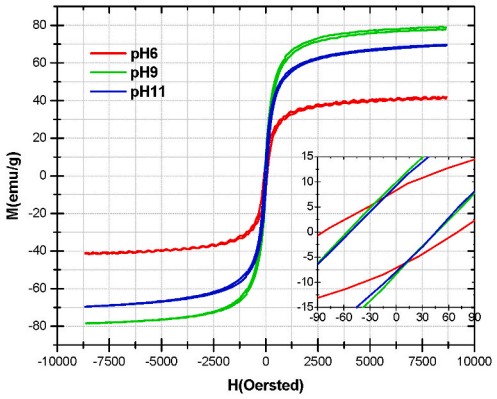

Fig. 3. VMS of samples. Magnetic moment vs the applied magnetic field.

3.2. Experimental design results

3.2.1. Effects on NP

The average diameters of all resulting nanoparticles ranged from 7.4 to 12.8 nm, as determined from the TEM images. Using the presented statistical tool we obtained the estimated effects and interactions of the selected parameters. We use the Pareto Chart of the standardized effects (Fig. 4). In this graph, the effects are represented as horizontal bars, in decreasing order of importance. In addition, a vertical blue line is displayed. Crossing this line with an effect signifies a significant difference from zero with 95 % confidence. Thus, it can be seen that the relationship between V_{NH4} and T_{res} is the most important factor in determining the NP_{size}. Moreover, the greater the correlation value, the bigger the size of the nanoparticles. The explanation rests on the fact that the lower the V_{NH4} the longer it takes for the reaction to come to completion. As a result, less subsequent T_{res} is required for the reaction to reach completion.

Taking into account the aforementioned interrelationship, observing the estimated response surface of Fig. 5, it is possible to predict that the largest nanoparticle size will be obtained when both V_{NH4} and T_{res} are at their minimum values. This means that the aforementioned intermediate times, relative to V_{NH4}, favor particle formation and growth to a greater extent than T_{res}. Furthermore, the rapid addition of the ammonia solution to the reaction solution favors continuous nucleation with respect to growth, thus allowing the formation of small particles [27], and a slow addition of the base allows to promote growth with respect to nucleation. Thus, Three would correspond mostly to time associated with the continuity of particle growth rather than particle nucleation.

From the XRD patterns, it was observed that all the resulting nanoparticles had average diameters between 7.5 and 17.8 nm. The Pareto Chart of the standardized effects (Fig. 6) shows that the interrelationship between V_{NH4} and T_{res} is the most important factor in determining the NP_{XRD}. The higher the value of V_{NH4} and T_{res} interrelationship, the larger the nanoparticle size.

Although it is possible to observe a difference between the sizes obtained by the two analysis systems, particularly visible towards the larger sizes, it is possible to confirm that the main dependence is related to the interrelation between V_{NH4} and T_{res}. The similarity of the low size values between the two measurement systems confirms that the peak broadening is essentially due to size effects and that microtensions can be neglected. The difference in larger sizes can be explained by considering a slight broadening of the diffraction peaks due to a partial shift caused by partial oxidation of magnetite. Something similar has been proposed earlier [28] and will be corroborated later in this article.

The results of the model obtained through experimental design are presented in Eq. (4).The adjusted equation predicts NP_{size} values between 8.6 and 14.1 nm.

With this achievable size range, we have nanoparticles that at least double their specific surface area, which allows for size management to optimize the specific surface area according to the needs of each application.

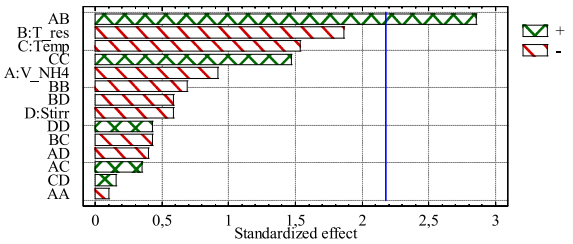

Fig. 4. Standardized Pareto chart for NP_{size}. Parameters of interest: (A) V_NH4, alkalizing drip rate; (B) T_res, reaction time; (C) Temp, temperature; and (D) Stirr, stirring rate.

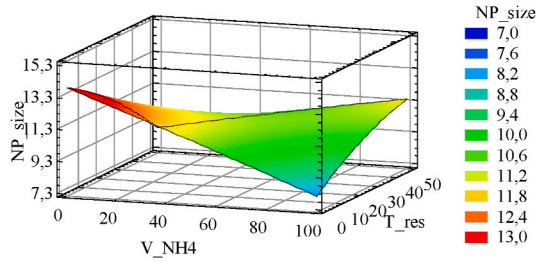

Fig. 5. Estimated response surface of NP_{size} with Temp and Stirr set to 60 and 600 respectively.

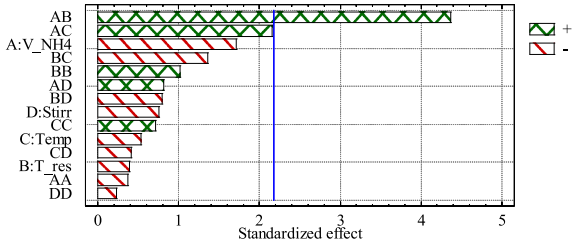

Fig. 6. Standardized Pareto chart for NP_{XRD}. Parameters of interest: (A) V_NH4, alkalizing drip rate; (B) T_res, reaction time; (C) Temp, temperature; and (D) Stirr, stirring rate.

$$NP_{size} = 25.4 - 0.29V_{NH4} - 0.18T_{res} - 0.08Temp + 4.05556e^{-3}Stirr - 1.82292e^{-4}V_{NH4}^2 + 5e^{-3}V_{NH4}T_{res} + 1.64583e^{-3}V_{NH4}Temp + 6.25e^{-5}V_{NH4}Stirr + 2.02083e^{-3}T_{res}^2 - 2.08333e^{-3}T_{res}Temp - 1.20833e^{-4}T_{res}Stirr + 6.34259e^{-4}Temp^2 - 416667e^{-5}TempStirr - 1.99074e^{-6}Stirr^2 \quad (4)$$

3.2.2. *Effects on disp*

Assuming a size dispersion dependent on the NP obtained, expressed as a percentage thereof, all the design results correspond to dispersions between 23.9 and 43.4 %. In this case, the Pareto Chart of the standardized effects (Fig. 7) shows that the square of V_{NH4} is the most important factor determining the Disp. The higher the value of this correlation, the greater the dispersion of the nanoparticles obtained.

Considering this and observing its effects in Fig. 8, it is possible to predict that the minimum dispersion is obtained when V_{NH4} is at its middle value, around 50 ml/h. This means that a medium value of V_{NH4} favors the homogeneous nucleation and growth of the particles. Abruptly adding the base solution can cause pH inhomogeneity in the reaction medium before complete mixing, which alters the reaction rate and pathway [23], favoring particle nucleation over growth. Conversely, adding the base solution very slowly favors particle growth over nucleation.

The results of the model obtained are shown in Eq. (5). The adjusted equation predicts Disp values between 15.7 and 45.6 %, and can be optimized according to the needs of the application.

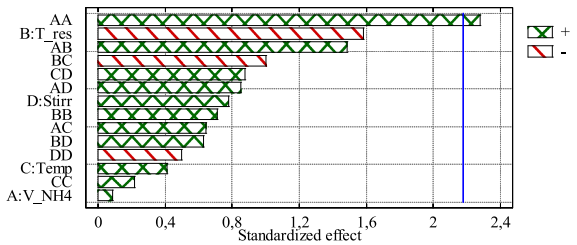

Fig. 7. Standardized Pareto chart for Disp. Parameters of interest: (A) V_NH4, alkalizing drip rate; (B) T_res, reaction time; (C) Temp, temperature; and (D) Stirr, stirring rate.

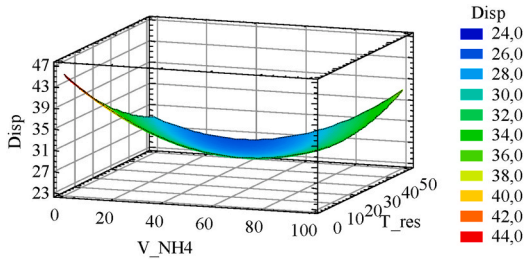

Fig. 8. Estimated response surface of Disp with Temp and Stirr set to 60 and 600 respectively.

$$Disp = 53.1458 - 0.532723\,V_{NH4} - 0.408443T_{res} - 0.11012Temp - 0.0111532Stirr + 260391e^{-3}V_{NH4}^2 + 3.91326e^{-3}V_{NH4}T_{res} + 1.12947e^{-3}V_{NH4}Temp + 1.49685e^{-4}V_{NH4}Stirr + 3.24718e^{-3}T_{res}^2 - 3.51866e^{-3}T_{res}Temp + 2.21247e^{-4}T_{reac}Stirr + 4.3935e^{-4}Temp^2 + 2.05116e^{-4}TempStirr - 1.01027e^{-5}Stirr^2 \quad (5)$$

3.2.3. *Effects on aglo*

The agglomeration of the nanoparticles was qualitatively analyzed in relation to their total size observed in the TEM images, using an arbitrary scale from 0 to 10. From the results, an analysis of the effect of the parameters was also performed. According to Fig. 9, the level of particle agglomeration is primarily determined by the interaction between V_{NH4} and T_{res}. A lower value of this relationship leads to smaller Aglo.

Observing the response surface in Fig. 10, it is possible to conclude that the synthesis time is the parameter with the highest incidence in the agglomeration of the nanoparticles. This in turn implies that agglomeration is inversely related to particle size, reaching the minimum when V_{NH4} and T_{res} are at their minimum values.

The resulting model is shown in Eq. (6). With this model Aglo values can be optimized as a function of the application.

$$Aglo = -8.46354 + 0.339583V_{NH4} + 0.121875T_{res} + 0.105556Temp + 4.375e^{-3}Stirr - 2.60417e^{-4}V_{NH4}^2 - 4.0625e^{-3}V_{NH4T_{res}} - 1.25e^{-3}V_{NH4}Temp - 1.45833e^{-4}V_{NH4}Stirr - 1.04167e^{-4}T_{res}^2 + 1.25e^{-3}T_{res}Temp - 1.25e^{-4}T_{res}Stirr - 1.43519e^{-3}Temp^2 + 1.66667e^{-4}TempStirr + 9.25926E^{-7}Stirr^2 \quad (6)$$

So far, we can say that if we want low dispersion and less agglomerated nanoparticles, the parameters to use during the synthesis would be with low V_{NH4} and T_{res}, without the values of Temp or Stirr having a greater incidence. This could be very good for application cases where there is no option to increase the temperature, either for feasibility or cost savings.

3.2.4. *Effects on M_s*

From the VSM results, it was observed that all the nanoparticles have superparamagnetic behavior with M_s between 40.2 and 72 emu/gr. All of these values are excellent as they facilitate the effortless collection of all nanoparticles using a standard magnet in just one step [26]. Using the statistical effects and interactions (Fig. 11), it is possible to observe that the interrelation between V_{NH4} and T_{res} is the most important factor in determining the M_s. Furthermore, the higher the value of said interrelation, the greater the saturation of the magnetization. This agrees with previous research as larger sizes of magnetite nanoparticles within the range where superparamagnetic behavior occurs exhibit greater saturation magnetization [24,29].

In fact, observing the response surface in Fig. 12, it is possible to notice that it is very similar to that observed for NP_{size}, impling that the Ms is directly related to the NP. The explanation of this will be the subject of discussion later in this article, after the topic of nanoparticle stoichiometry has been discussed.

The model results obtained are shown in Eq. (7). The adjusted equation predicts M_s values between 46 and 76.2 emu/gr, and can be

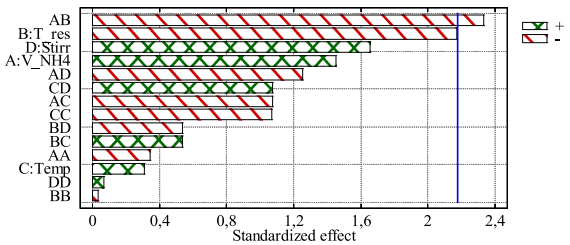

Fig. 9. Standardized Pareto chart for Aglo. Parameters of interest: (A) V_NH4, alkalizing drip rate; (B) T_res, reaction time; (C) Temp, temperature; and (D) Stirr, stirring rate.

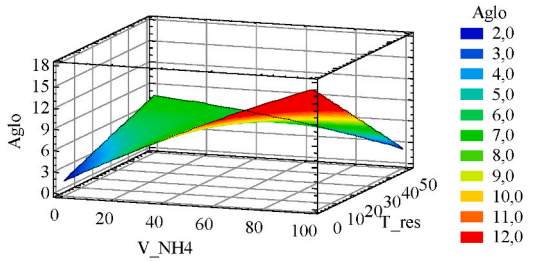

Fig. 10. Estimated response surface of Aglo with Temp and Stirr set to 60 and 600 respectively.

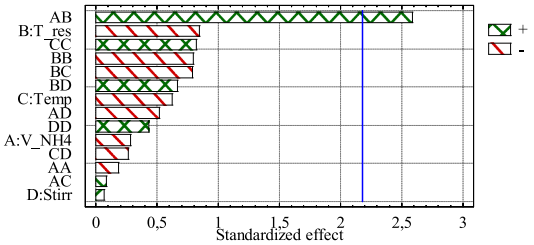

Fig. 11. Standardized Pareto chart for M_s. Parameters of interest: (A) V_NH4, alkalizing drip rate; (B) T_res, reaction time; (C) Temp, temperature; and (D) Stirr, stirring rate.

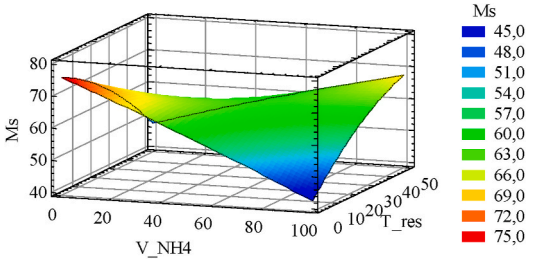

Fig. 12. Estimated response surface of M_s with Temp and Stirr set to 60 and 600 respectively.

optimized depending on the application.

$$M_s = 83.6529 - 0.230365V_{NH4} - 0.232708T_{res} - 0.174792Temp - 0.0140556Stirr - 3.25521e^{-4}V_{NH4}^2 + 0.0106875V_{NH4}T_{res} + 2.29167e^{-4}V_{NH4}Temp - 1.41667e^{-4}V_{NH4}Stirr - 5.70833e^{-3}T_{res}^2 - 4.33333e^{-3}T_{res}Temp + 3.66667e^{-4}T_{res}Stirr + 2.60185e^{-3}Temp^2 - 9.72222e^{-5}TempStirr + 1.36574e^{-5}Stirr^2 \quad (7)$$

For example, how to obtain 10 nm nanoparticles with almost 80 emu/gr and almost no temperature application, which would be ideal for industrial applications, has already been demonstrated at this point.

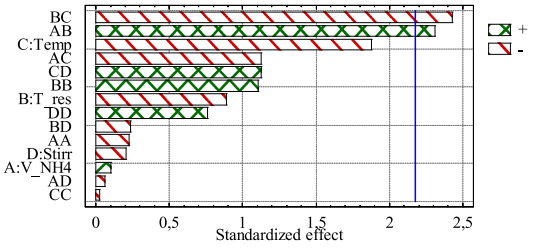

Fig. 13. Standardized Pareto chart for Mr. Parameters of interest: (A) V_NH4, alkalizing drip rate; (B) T_res, reaction time; (C) Temp, temperature; and (D) Stirr, stirring rate.

3.2.5. Effects on M_r

In the case of Mr, values between 1.1 and 5.4 emu/gr were obtained, which are quite low values and allow us to determine that MNPs are obtained that maintain their superparamagnetic properties. This enables their quick redistribution after the external magnetic field is eliminated [30]. Using the statistical effects and interactions (Fig. 13) it is possible to observe that the T_{res} x Temp and V_{NH4} x T_{res} interrelationships are the most important factors in determining the M_r. Moreover, the lower the value of T_{res} x Temp and the higher the value of V_{NH4} x T_{res} interrelationships, the higher the remnant magnetization. The second interaction in turn implies that Mr depends on Ms and therefore on the particle size.

Considering this and observing its effects in Fig. 14, it can be predicted that the minimum remnant magnetization is obtained when T_{res} and Temp are in their maximum values. This means that the high temperature and the long reaction time during the process favor the stability of the superparamagnetic properties of the nanoparticles. This could be explained considering that the reaction time favors particle growth and the temperature facilitates structural ordering, thus allowing its correct and complete formation.

The resulting model is shown in Eq. (8). The adjusted equation predicts M_r values from 0.8 to 6.9 emu/gr, that can be optimized depending on the needs of the application.

$$\begin{aligned} M_r = {} & 5.14271 - 5.72917e^{-3}V_{NH4} - 0.0198958T_{res} + 0.0252083Temp - 6.45139e^{-3}Stirr - 5.20833e^{-5}V_{NH4}^2 + 1.21875e^{-3}V_{NH4}T_{res} \\ & - 3.95833e^{-4}V_{NH4}Temp - 2.08333e^{-6}V_{NH4}Stirr + 1.01042e^{-3}T_{res}^2 - 1.70833e^{-3}T_{res}Temp - 1.66667e^{-5}T_{res}Stirr - 9.25926e^{-6}Temp^2 \\ & + 5.27778e^{-5}TempStirr + 3.10185e^{-6}Stirr^2 \end{aligned} \tag{8}$$

3.2.6. Effects on H_c

In the case of H_c, values between 8.9 and 37.2 Oersted were obtained, which is very good in all cases because they are very small values, which ensures the obtaining of superparamagnetic nanoparticles because very small coercivity is often regarded as a signature of superparamagnetism [31]. The Pareto Chart of the standardized effects (Fig. 15) shows that, as in the case of M_r, there is a strong dependence on M_s, as well as the interrelation between T_{res} and Temp, but there is also an inverse relationship with Temp.

Observing the response surface in Fig. 16, it is possible to establish that the minimum coercitivity is obtained when T_{res} and Temp are in their maximum values. This confirm what was mentioned above, that a high temperature during the process and a long reaction time favor the completion of the reaction and thus the stability of the superparamagnetic properties of the nanoparticles.

The resulting model obtained are shown in Eq. (9). The adjusted equation predicts H_c values from 5 to 48 Oersted that can be optimized depending on the application.

$$\begin{aligned} H_c = {} & 44.3417 - 0.0552083V_{NH4} - 0.297292T_{res} + 0.0266667Temp - 0.0537361Stirr - 4.0625e^{-4}V_{NH4}^2 + 8.5e^{-3}V_{NH4}T_{res} \\ & - 2.5e^{-3}V_{NH4}Temp - 3.33333e^{-5}V_{NH4}Stirr + 9.78125e^{-3}T_{res}^2 - 0.0119167T_{res}Temp - 1.125e^{-4}T_{res}Stirr + 5.41667e^{-4}Temp^2 \\ & + 4.58333e^{-4}TempStirr + 2.44444e^{-5}Stirr^2 \end{aligned} \tag{9}$$

3.2.7. Effects on $Fe_{3-x}O_4$

Most of the authors do not clarify the obtaining of magnetite or maghemite, but simply assume the phase obtained [32]. This is because it is difficult to distinguish these phases using classical characterizations. Nevertheless, there are authors who have shown that when the size is less than 20 nm, the magnetic hyperfine structure can be described as magnetite with a slight deviation from the stoichiometry and the overall formula can be written as $Fe_{3-x}O_4$ [32,33]. Considering this, we perform an XRD analysis of the obtained oxide nanoparticles to study possible variations and their possibility of control. Values between 2.886 and 3 were obtained for the relative deviation from the stoichiometry of Fe_3O_4, (3-x). The Pareto diagram of the standardized effects (Fig. 17) shows that T_{res}, Temp and V_{NH4} are determining factors in the stoichiometry of the magnetite obtained. The higher the values, in the presented order, the lower the stoichiometric variation obtained.

Considering the above effects and looking at the estimated response surface of Fig. 18, it can be seen that the most correct stoichiometric magnetite is obtained when T_{res}, Temp and V_{NH4} are at their maximum values. This implies that the stoichiometric deviation of the resulting magnetite decreases with increasing particle size and formation temperature. Furthermore, it is possible to explain that T_{res} is the most important factor, since it is precisely the time that favors growth over particle formation. This in turn can explain what has been observed for the magnetization, since if the larger the size, the more complete the stoichiometry, the closer its magnetic behavior will be to that of magnetite, and if its stoichiometry is more displaced, its magnetic behavior will increasingly resemble that of maghemite.

The model results obtained are shown in Eq. (10). The adjusted equation predicts $Fe_{3-x}O_4$ with 3-x from 2.8 to 3, that can be optimized depending on the application.

$$\begin{aligned} 3 - x = {} & 2.73885 + 8.15625e^{-4}V_{NH4} + 3.92708e^{-4}T_{res} + 2.01181e^{-3}Temp + 1.39375e^{-4}Stirr - 1,04167e^{-7}V_{NH4}^2 - 1.34375e^{-5}V_{NH4}T_{res} \\ & - 8.125e^{-6}V_{NH4}Temp + 9,79167e^{-7}V_{NH4}Stirr + 3.33333e^{-5}T_{res}^2 - 4.41667e^{-5}T_{res}Temp + 4.41667e^{-6}T_{res}Stirr \\ & + 1.92593e^{-5}Temp^2 - 2.55556e^{-6}TempStirr - 1,26852e^{-7}Stirr^2 \end{aligned} \tag{10}$$

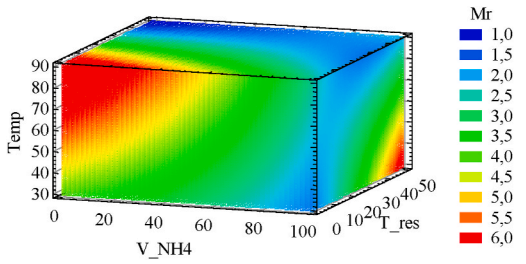

Fig. 14. Estimated response surface mesh plot of Mr with Stirr set to 600.

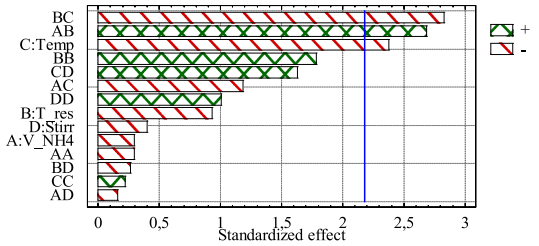

Fig. 15. Standardized Pareto chart for H_c. Parameters of interest: (A) V_NH4, alkalizing drip rate; (B) T_res, reaction time; (C) Temp, temperature; and (D) Stirr, stirring rate.

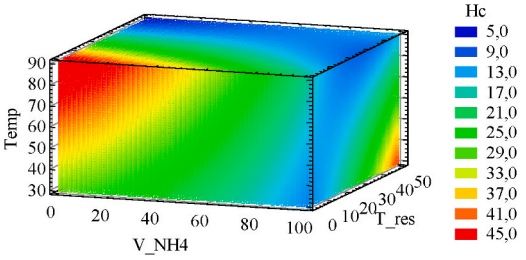

Fig. 16. Estimated response surface mesh plot of H_c with Stirr set to 600.

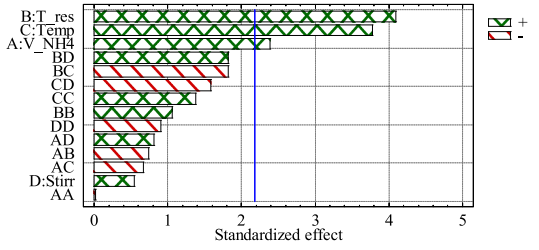

Fig. 17. Standardized Pareto chart for (3-x). Parameters of interest: (A) V_NH4, alkalizing drip rate; (B) T_res, reaction time; (C) Temp, temperature; and (D) Stirr, stirring rate.

3.2.8. Validation experiments

Finally, three validation experiments were carried out (Table 2). These experiments were chosen to be interesting to verify because they imply extremes in the parameters that turned out to be the most important.

The first case M1 corresponds to extreme maximum V_{NH4}. The result obtained for the NP was 12.6 nm, which corresponds quite well to the 13.1 that our model would predict for this case, with less than 4 % of error. In parallel, the Disp result of 35.1 % while the model predict 35.4 %, less than 1 % of error. For the M2 case, we extreme de minimum T_{res} value and use a low V_{NH4} to obtain a high value of Ms and high stoichiometry of the resulting magnetite. According to the corresponding model, the Ms should be of 74.3 emu/gr, and the experiment results in a value of 69.3 emu/gr, which is equivalent to 7.2 % of error. In parallel, the (3-x) result 2.939 while the model predict 2.887, 1.8 % of error. In the last case M3 we prove a extreme mínimum value of V_{NH4}, which give us very good

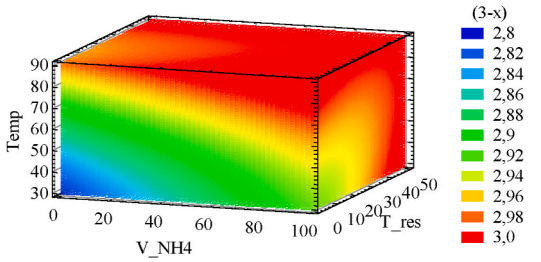

Fig. 18. Estimated response surface mesh plot of (3-x) with Stirr set to 600.

Table 2
Validation experiments parameters.

	PH	V_NH4	T_res	Temp	Stirr
M1	9	100	30	77	600
M2	9	10	0	50	300
M3	9	2	50	50	500

camparative results, since the NP varied by only 0.9 % (11.2 exp. vs 11.4 model) and the Ms by 26 % (65.3 exp. vs 48.3 model).

These results are completely satisfactory for the control of the properties of the resulting nanoparticles by managing the synthesis parameters. Even more so considering that in the case of magnetic properties, where we have the greatest differences, specifically at V_{NH4} extreme values, is where probably the speed of addition of the base solution would make it possible to modify which reaction pathway is dominant, thus favoring the obtaining of one oxide.

It should be noted that although this article did not carry out a complete study of the efficiency of the synthesis, the samples made after optimization of the parameters show a visually complete recovery of the material with a totally transparent remaining solution.

4. Conclusions

A statistical technique, rooted in "Design of Experiments" (DoE), was employed to design a reaction setup for co-precipitating specific iron oxide nanoparticles. The primary interest was to determine how reaction conditions affected the size and saturation magnetization of the output. The nanoparticles synthesized underwent analysis through XRD, TEM, and VSM methods.

The synthesis yields mainly spherical magnetite morphology, with pH as the decisive factor in the formation process. All samples display superparamagnetic behavior at room temperature. Successful synthesis of iron oxide nanoparticles is achieved in the size range of 7.4–12.8 nm with dispersion in the range of 21.4–42.1%. The nanoparticles demonstrate varying magnetic properties, featuring saturation magnetization ranging from 46 to 78 emu/g, a remarkably low coercive field, and remanent magnetization ranging from 7 to 37 Oe and 1–5 emu/g, respectively. The oxide nanoparticles are characterized as Fe3-xO4 with the alkali drop rate serving as the critical parameter for modifying "x." Overall, the alkalization drop rate and reaction time can be manipulated to control particle size and magnetic properties. The magnetic properties vary due to both size and composition, as the oxidation rate increases with decreasing size.

Finally, it has been demonstrated that optimizing the achieved models enables a selective choice of the synthesis parameters, depending on the preferred characteristics of the final nanoparticles. This creates new opportunities for more precise investigations in each application case.

Data availability

Data will be available on request.

CRediT authorship contribution statement

María José Inestrosa-Izurieta: Conceptualization, Data curation, Formal analysis, Investigation, Methodology, Project administration, Supervision, Validation, Visualization, Writing – original draft, Writing – review & editing, Funding acquisition. **Diego Vilches:** Investigation, Methodology. **Julio I. Urzúa:** Funding acquisition, Supervision.

Declaration of competing interest

The authors declare that they have no known competing financial interests or personal relationships that could have appeared to influence the work reported in this paper.

Acknowledgments

This research has not receive any grants from public, commercial, or nonprofit funding agencies. The Chilean Nuclear Energy Commission provided resources to support this work. The authors express their gratitude to the Center for the Development of Nanoscience and Nanotechnology (CEDENNA) staff for their assistance with TEM and VSM measurements.

References

[1] P. Sangaiya, R. Jayaprakash, A review on iron oxide nanoparticles and their biomedical applications, J. Supercond. Nov. Magn. 31 (2018) 3397–3413, https://doi.org/10.1007/s10948-018-4841-2.
[2] S. Ansari, E. Ficiarà, F. Ruffinatti, I. Stura, M. Argenziano, O. Abollino, R. Cavalli, C. Guiot, F. D'Agata, Magnetic iron oxide nanoparticles: synthesis, characterization and functionalization for biomedical applications in the central nervous system, Materials 12 (2019) 465, https://doi.org/10.3390/ma12030465.
[3] H. Han, W. Sun, W. Sun, Y. Hu, Magnetic separation of impurities from hydrometallurgy solutions and waste water using magnetic iron ore seeding, Iron Ores, IntechOpen (2021) 13, https://doi.org/10.5772/intechopen.93728.
[4] L. Molina-Calderón, C. Basualto-Flores, V. Paredes-García, D. Venegas-Yazigi, Advances of magnetic nanohydrometallurgy using superparamagnetic nanomaterials as rare earth ions adsorbents: a grand opportunity for sustainable rare earth recovery, Sep. Purif. Technol. 299 (2022), 121708, https://doi.org/10.1016/j.seppur.2022.121708.
[5] M. Singh, S. Dhiman, N. Debnath, S. Das, Magnetic nanoparticles and their application in sustainable environment, in: Sustain. Nanotechnol. Environ. Remediat., Elsevier, 2022, pp. 457–483, https://doi.org/10.1016/B978-0-12-824547-7.00007-2.
[6] A. Misra, C. Zambrzycki, G. Kloker, A. Kotyrba, M.H. Anjass, I. Franco Castillo, S.G. Mitchell, R. Güttel, C. Streb, Water purification and microplastics removal using magnetic polyoxometalate-supported ionic liquid phases (magPOM-SILPs), Angew. Chem. Int. Ed. 59 (2020) 1601–1605, https://doi.org/10.1002/anie.201912111.
[7] H.M. Joshi, M. De, F. Richter, J. He, P. V Prasad, V.P. Dravid, Effect of silica shell thickness of Fe_3O_4–SiO_x core–shell nanostructures on MRI contrast, J. Nanoparticle Res. 15 (2013) 1448, https://doi.org/10.1007/s11051-013-1448-1.
[8] M. Wegmann, M. Scharr, Synthesis of magnetic iron oxide nanoparticles, in: Precis. Med., Elsevier, 2018, pp. 145–181, https://doi.org/10.1016/B978-0-12-805364-5.00008-1.
[9] S.L.C. Pinho, J. Sereno, A.J. Abrunhosa, M. Delville, J. Rocha, L.D. Carlos, C.F.G.C. Geraldes, Gd- and Eu-loaded iron Oxide@Silica core–shell nanocomposites as trimodal contrast agents for magnetic resonance imaging and optical imaging, Inorg. Chem. 58 (2019) 16618–16628, https://doi.org/10.1021/acs.inorgchem.9b02655.
[10] U. Condomitti, S. Almeida, A. Silveira, F. de Melo, H. Toma, Green processing of strategic elements based on magnetic nanohydrometallurgy, J. Braz. Chem. Soc. 29 (2018) 948–959, https://doi.org/10.21577/0103-5053.20180009.
[11] R.C. Popescu, E. Andronescu, B.S. Vasile, Recent advances in magnetite nanoparticle functionalization for nanomedicine, Nanomaterials 9 (2019) 1–31, https://doi.org/10.3390/nano9121791.
[12] M.I. Dar, S.A. Shivashankar, Single crystalline magnetite, maghemite, and hematite nanoparticles with rich coercivity, RSC Adv. 4 (2014) 4105–4113, https://doi.org/10.1039/c3ra45457f.
[13] H. Roth, S.P. Schwaminger, M. Schindler, F.E. Wagner, S. Berensmeier, Influencing factors in the CO-precipitation process of superparamagnetic iron oxide nano particles: a model based study, J. Magn. Magn Mater. 377 (2015) 81–89, https://doi.org/10.1016/j.jmmm.2014.10.074.
[14] K. Petcharoen, A. Sirivat, Synthesis and characterization of magnetite nanoparticles via the chemical co-precipitation method, Mater. Sci. Eng. B. 177 (2012) 421–427, https://doi.org/10.1016/j.mseb.2012.01.003.
[15] S. Kumar, M. Kumar, A. Singh, Synthesis and characterization of iron oxide nanoparticles (Fe2O3, Fe3O4): a brief review, Contemp. Phys. 62 (3) (2021) 144–164, https://doi.org/10.1080/00107514.2022.2080910.
[16] R. Massart, Preparation of aqueous magnetic liquids in alkaline and acidic media, IEEE Trans. Magn. 17 (1981) 1247–1248.
[17] S. Goktas, M.D. Köse, O. Bayraktar, A screening experimental design to develop high extraction yield of flavonoids in Ginkgo biloba leaves, J. Pharm. Appl. Chem. 3 (2017) 33–39, https://doi.org/10.18576/jpac/030104.
[18] X. Peng, G. Yang, Y. Shi, Y. Zhou, M. Zhang, S. Li, Box–Behnken design based statistical modeling for the extraction and physicochemical properties of pectin from sunflower heads and the comparison with commercial low-methoxyl pectin, Sci. Rep. 10 (2020) 3595, https://doi.org/10.1038/s41598-020-60339-1.
[19] H. Dhawan, S. Upadhyayula, D.K. Sharma, Design of experiments to optimize the extraction parameters of a power grade Indian coal, Int. J. Coal. Sci. Technol. 5 (2018) 417–429, https://doi.org/10.1007/s40789-018-0216-3.
[20] C. Da Silva Sousa Jr., M. Nascimento, L. Yokoyama, O. Galvão Caldas Da Cunha, Experimental design in solvent extraction: a study for divalent metals separation in D2EHPA/isoparaffin system, Engineering 4 (2012) 816–825, https://doi.org/10.4236/eng.2012.411104.
[21] NIST/SEMATECH E-Handbook of Statistical Methods, 2013. https://www.itl.nist.gov/div898/handbook/pri/section3/pri3.htm. https://www.itl.nist.gov/div898/handbook/.
[22] T. Ahn, J.H. Kim, H.M. Yang, J.W. Lee, J.D. Kim, Formation pathways of magnetite nanoparticles by coprecipitation method, J. Phys. Chem. C 116 (2012) 6069–6076, https://doi.org/10.1021/jp211843g.
[23] J. Baumgartner, A. Dey, P.H.H. Bomans, C. Le Coadou, P. Fratzl, N.A.J.M. Sommerdijk, D. Faivre, Nucleation and growth of magnetite from solution, Nat. Mater. 12 (2013) 310–314, https://doi.org/10.1038/nmat3558.
[24] Z. Ra'ad, N.K.A. Alsahib, L.Q. Al-Karam, Synthesis of iron oxide nanoparticles using precipitation method with different pH values, AIP Conf. Proc. 2372 (2021), 020009, https://doi.org/10.1063/5.0067088.
[25] J. Jolivet, C. Chanéac, E. Tronc, Iron oxide chemistry. From molecular clusters to extended solid networks, Chem. Commun. 5 (2004) 477–483, https://doi.org/10.1039/B304532N.
[26] C. Basualto, J. Gaete, L. Molina, F. Valenzuela, C. Yañez, J.F. Marco, Lanthanide sorbent based on magnetite nanoparticles functionalized with organophosphorus extractants, Sci. Technol. Adv. Mater. 16 (2015), 035010, https://doi.org/10.1088/1468-6996/16/3/035010.
[27] M.C. Mascolo, Y. Pei, T.A. Ring, Room temperature Co-precipitation synthesis of magnetite nanoparticles in a large ph window with different bases, Materials 6 (2013) 5549–5567, https://doi.org/10.3390/ma6125549.
[28] J. Mürbe, A. Rechtenbach, J. Töpfer, Synthesis and physical characterization of magnetite nanoparticles for biomedical applications, Mater. Chem. Phys. 110 (2008) 426–433, https://doi.org/10.1016/j.matchemphys.2008.02.037.
[29] X. Wen, J. Yang, B. He, Z. Gu, Preparation of monodisperse magnetite nanoparticles under mild conditions, Curr. Appl. Phys. 8 (2008) 535–541, https://doi.org/10.1016/j.cap.2007.09.003.
[30] I. Alfaro, L. Molina, P. González, J. Gaete, F. Valenzuela, J.F. Marco, C. Sáez, C. Basualto, Silica-coated magnetite nanoparticles functionalized with betaine and their use as an adsorbent for Mo(VI) and Re(VII) species from acidic aqueous solutions, J. Ind. Eng. Chem. 78 (2019) 271–283, https://doi.org/10.1016/j.jiec.2019.06.002.

[31] R.L. Andersson, L. Cabedo, M.S. Hedenqvist, R.T. Olsson, V. Ström, Superparamagnetic [sic] nanofibers by electrospinning, RSC Adv. 6 (2016) 21413–21422, https://doi.org/10.1039/c5ra27791d.

[32] M.D. Carvalho, F. Henriques, L.P. Ferreira, M. Godinho, M.M. Cruz, Iron oxide nanoparticles: the Influence of synthesis method and size on composition and magnetic properties, J. Solid State Chem. 201 (2013) 144–152, https://doi.org/10.1016/j.jssc.2013.02.024.

[33] J. Santoyo Salazar, L. Perez, O. De Abril, L. Truong Phuoc, D. Ihiawakrim, M. Vazquez, J.M. Greneche, S. Begin-Colin, G. Pourroy, Magnetic iron oxide nanoparticles in 10-40 nm range: composition in terms of magnetite/maghemite ratio and effect on the magnetic properties, Chem. Mater. 23 (2011) 1379–1386, https://doi.org/10.1021/cm103188a.